reproduced by permission of the AAS

THE ASTROPHYSICAL JOURNAL, ~~602:000–000, 2004 February 20~~ 2004, April 10.
© 2004. The American Astronomical Society. All rights reserved. Printed in U.S.A.

# MAGNETOHYDRODYNAMIC ACCRETION FLOWS: FORMATION OF MAGNETIC TOWER JET AND SUBSEQUENT QUASI–STEADY STATE

Y. KATO AND S. MINESHIGE
Yukawa Institute for Theoretical Physics, Kyoto University, Kyoto 606-8502, Japan

AND

K. SHIBATA
Kwasan Observatory, Kyoto University, Yamashina-Ku, Kyoto 607-8471, Japan
*Received 2003 July 15; accepted 2003 November 7*

## ABSTRACT

We present three-dimensional magnetohydrodynamic (MHD) simulations of radiatively inefficient accretion flow around black holes. General relativistic effects are simulated by using the pseudo-Newtonian potential. We start calculations with a rotating torus threaded by localized poloidal magnetic fields with plasma-$\beta$, a ratio of the gas pressure to the magnetic pressure, $\beta = 10$ and 100. When the bulk of torus material reaches the innermost region close to a central black hole, a magnetically driven jet emerges. This magnetic jet is derived by vertically inflating toroidal fields ("magnetic tower") and has a two-component structure: low-$\beta$ ($\lesssim 1$) plasmas threaded with poloidal (vertical) fields are surrounded by those with toroidal fields. The collimation width of the jet depends on external pressure, the pressure of ambient medium; the weaker the external pressure is, the wider and the longer lasting becomes the jet. Unless the external pressure is negligible, the bipolar jet phase ceases after several dynamical timescales at the original torus position and a subsequent quasi–steady state starts. The black hole is surrounded by a quasi-spherical zone with highly inhomogeneous structure in which toroidal fields are dominant except near the rotation axis. Mass accretion takes place mainly along the equatorial plane. Comparisons with other MHD simulation results and observational implications are discussed.

*Subject headings:* accretion, accretion disks — black hole physics — ISM: jets and outflows — MHD — relativity

## 1. INTRODUCTION

The study of accretion disk structure has a long research history, yet fundamental structure has not become clear. The standard disk model established in the early 1970s has been very successful in describing the high/soft states of Galactic black hole (BH) candidates (see, e.g., Ebisawa 1999), but their low/hard state characterized by power-law–type spectra was problematic to the standard model. Alternative disk models that account for high-energy emissions from X-ray binaries (XRBs) and active galactic nuclei (AGNs) have been extensively discussed and the base of a distinct type of disk models has been constructed by Narayan & Yi (1994), which turned out to be the same model as that proposed by Ichimaru (1977). This notion is now referred to as "advection-dominated accretion flow" (ADAF; see reviews by Narayan, Mahadevan, & Quataert 1998; Kato, Fukue, & Mineshige 1998).

The key relation to discriminate the standard and ADAF solutions resides in the energy equation of accretion disks, $Q_{\rm adv} = Q^{-}_{\rm vis} - Q^{+}_{\rm rad}$, with, from the left, the advection term representing energy transport carried by accreting material, the viscous heating term, and the radiative cooling term, respectively. This relation yields three distinct solutions, depending on the final forms of accretion energy. Accretion energy goes to radiation in a standard disk so that the disk becomes cool and shines bright. In an optically thin ADAF, in contrast, accretion energy is converted to internal energy of gas. ADAF is thus characterized by high temperature and low emissivity. The third is a hot optically thin cooling-dominated disk (Shapiro, Lightman, & Eardley 1976) that is thermally unstable.

Although the ADAF model is quite successful in reproducing the hard spectra of Galactic BH candidates, as well as those of low-luminosity AGNs and our Galactic center source, Sgr A*, it comprises a serious problem. The original optically thin ADAF model has been constructed basically in a vertically one-zone approximation. In other words, it was formulated in one (radial) dimension, although multidimensional flow patterns seem to be essential. In this regard, Narayan & Yi (1994) already made two important pieces of predictions: possible occurrence of convection (in the radial direction) and outflows. Since radiative cooling is inefficient, entropy of accreting gas should monotonically increase toward a BH (i.e., in the direction of gravity), a condition for a convection. Further, the self-similar model points to an advection-dominated flow having a positive Bernoulli parameter, Be, meaning that matter is gravitationally unbound and can form outflows.

Actually, two- or three-dimensional hydrodynamical simulations exhibit complex flow patterns (Stone, Pringle, & Begelman 1999; see also Igumenshchev & Abramowicz 2000; Igumenshchev, Abramowicz, & Narayan 2000). Taking this fact into account, several authors proposed alternative models with some modifications to the ADAF picture. Blandford & Begelman (1999), for example, constructed a model of adiabatic inflow/outflow solution (ADIOS) so as to incorporate the emergence of strong jets in the one-dimensional scheme. Convection-dominated accretion flow (CDAF; Quataert & Gruzinov 2000; Narayan 2002), on the other hand, considers the significant effects of large-scale convective motion. They especially point out that angular momentum is carried not outward (as in the viscous disk) but inward, while energy is

transported outward in CDAF. These are the main products in the second stage of research of hot accretion flow (or radiatively inefficient flow).

Yet, this is not the end of the story. One may well ask what an ADAF model can properly treat since it is a time-stationary, one-dimensional, alpha model. Note that the ADIOS and CDAF models also share that problem: they also cannot properly treat the accretion flows, unlike a full numerical simulation.

Furthermore, a hydrodynamical approach seems to be totally inappropriate in radiatively inefficient flow. Rather, we expect that magnetic fields play crucial roles in hot accretion flows; disks in the low/hard state could be low-$\beta$ disk coronae, in which magnetic pressure exceeds gas pressure (Mineshige, Kusnose, & Matsumoto 1995); that is, the magnetohydrodynamic (MHD) approach is indispensable. To be more precise, the significance of magnetic fields is not restricted to radiatively inefficient flow but is also in a standard-type disk, since magnetic fields provide the source of disk viscosity as a consequence of magnetorotational instability (MRI; Balbus & Hawley 1991). Now we have entered the third stage of the research of hot accretion flow based on the multidimensional MHD simulations.

First global three-dimensional MHD simulations of accretion disks have been made by Matsumoto (1999). He calculated the evolution of magnetic fields and structural changes of a torus that is initially threaded by toroidal magnetic fields. In relation to the MHD accretion flow, we would like to remind readers that similar simulations had already been performed by many groups in the context of astrophysical jets, pioncered by Uchida & Shibata (1985; see also Shibata & Uchida 1986). They calculated the evolution of a disk threaded with vertical fields extending to infinity to see how a magnetic jet is produced. Hence, their simulations were more concerned with the jet structure and a disk only plays a passive role, but it is instructive to see how the disk behaves in those simulations. Since angular momentum can be very efficiently extracted from the surface of the accretion disks by the vertical fields, a surface avalanche produces anomalous mass accretion in those simulations. Thus, we need to be careful that the situation may depend on whether magnetic fields are provided externally or they are generated internally.

Many MHD disk simulations starting with locally confined fields have been published after 2000. Machida, Hayashi, & Matsumoto (2000) extended Matsumoto (1999) and studied the structure of MHD flow starting with initially toroidal, localized fields and found global low-$\beta$ filaments created in the turbulent accretion disk (see also Hawley 2000; Hawley & Krolik 2001). Machida, Matsumoto, & Mineshige (2001) have shown that its flow structure is very similar to those of CDAF in the sense of visible convective patterns and relatively flatter density profile ($\rho \propto r^{-1/2}$), which contrasts with $\rho \propto r^{-3/2}$ in ADAF. They conjectured that such flow pattern is driven by thermodynamic buoyant instabilities; however, Stone & Pringle (2001) established that it is most likely to be produced by the turbulence due to the MRI (see also Hawley, Balbus, & Stone 2001; Hawley 2001). Thus, the MRI is the fundamental process that converts gravitational energy into turbulent energy within the magnetized disk (see Balbus 2003 for a review).

Outflows also appear in MHD simulations starting with localized fields. Kudoh, Matsumoto, & Shibata (2002, hereafter KMS02), for example, have found the rising magnetic loop that behaves like a jet (see also Turner, Bodenheimer, & Różyczka 1999). They assert that the jet is collimated by a pinching force of the toroidal magnetic field and that its velocity is on order of the Keplerian velocity of the disk. Hawley & Balbus (2002, hereafter HB02) calculated the evolution of a torus with initial poloidal fields and found three well-defined dynamical components: a hot, thick, rotationally dominated, high-$\beta$ Keplerian disk; a surrounding hot, unconfined, low-$\beta$ coronal envelope; and a magnetically confined unbound high-$\beta$ jet along the centrifugal funnel wall (see also Kudoh, Matsumoto, & Shibata 1998; Stone & Pringle 2001; Hawley et al. 2001; Casse & Keppens 2002).

Recently, Igumenshchev, Narayan, & Abramowicz (2003, hereafter INA03) have reported that the flow structure with continuous mass and toroidal or poloidal field injection evolves through two distinct phases: an initial transient phase associated with a hot corona and a bipolar outflow, and a subsequent steady state, with most of the volume being dominated by a strong dipolar magnetic field. In addition, they also have argued that the accretion flow is totally inhibited by the strong magnetic field.

In the present study we performed three-dimensional MHD simulations of a rotating torus with the same initial condition as that of HB02, but adopting a different inner boundary condition than that of HB02. The aims of the present study are twofold: the first one is to examine how an MHD jet emerges from localized field configurations and what properties it has; the second one is to elucidate the dynamics of MHD accretion flow in radiation-inefficient regimes by means of long-term simulations and compare our results with previous ones. In § 2 we present basic equations and explain our models of three-dimensional global MHD simulation. We then present our results in the first phase of an evolving magnetic tower jet and in the second phase of a subsequent quasi–steady state in § 3. The final section is devoted to a brief summary and discussion.

## 2. OUR MODELS AND METHODS OF SIMULATIONS

We solve the basic equations of the resistive MHD in the cylindrical coordinates, $(r, \phi, z)$. General relativistic effects are incorporated by the pseudo-Newtonian potential (Paczyński & Wiita 1980), $\psi = -GM/(R - r_S)$, where $R\ [\equiv (r^2 + z^2)^{1/2}]$ is the distance from the origin and $r_S$ $(\equiv 2GM/c^2)$ is the Schwarzschild radius (with $M$ and $c$ being the mass of a BH and the speed of light, respectively). The basic equations are then written in a conservative form as follows:

$$\frac{\partial \rho}{\partial t} + \nabla \cdot (\rho \boldsymbol{v}) = 0, \tag{1}$$

$$\frac{\partial}{\partial t}(\rho \boldsymbol{v}) + \nabla \cdot \left(\rho \boldsymbol{v}\boldsymbol{v} - \frac{\boldsymbol{B}\boldsymbol{B}}{4\pi}\right) = -\nabla \left(p_{\rm gas} + \frac{B^2}{8\pi}\right) - \rho \nabla \psi, \tag{2}$$

$$\frac{\partial}{\partial t}\left(\epsilon + \frac{B^2}{8\pi}\right) + \nabla \cdot \left[(\epsilon + p_{\rm gas})\boldsymbol{v} + \frac{\boldsymbol{E}\boldsymbol{B}}{4\pi}\right] = -\rho \boldsymbol{v} \cdot \nabla \psi, \tag{3}$$

and

$$\frac{\partial \boldsymbol{B}}{\partial t} = -c\nabla \times \boldsymbol{E}, \tag{4}$$

where $\epsilon = \rho v^2/2 + p_{\rm gas}/(\gamma - 1)$ is the energy of the gas and $\boldsymbol{E} = -(\boldsymbol{v}/c) \times \boldsymbol{B} + (4\pi\eta/c^2)\boldsymbol{J}$ is Ohm's law. $\boldsymbol{J} = (c/4\pi)\nabla \times \boldsymbol{B}$ is the electric current. We fix the adiabatic index to be $\gamma = \frac{5}{3}$.

As to the resistivity, we assign the anomalous resistivity, which is used in many solar flare simulations (e.g., Yokoyama & Shibata 1994):

$$\eta = \begin{cases} 0 & \text{for } v_d < v_{\rm crit}, \\ \eta_{\rm max}\left[\left(\dfrac{v_d}{v_{\rm crit}}\right) - 1\right]^2 & \text{for } v_{\rm crit} < v_d < 2v_{\rm crit}, \\ \eta_{\rm max} & \text{for } v_d \geq 2v_{\rm crit}, \end{cases} \quad (5)$$

where $v_d \equiv |\boldsymbol{J}|/\rho$ is the electron drift velocity, $v_{\rm crit}$ is the critical velocity, over which anomalous resistivity turns on, and $\eta_{\rm max}$ is the maximum resistivity. In the present study we assign $v_{\rm crit} = 0.01$ (in the unit of $c$) and $\eta_{\rm max} = 10^{-3} c r_{\rm S}$; i.e., the magnetic Reynolds number is ${\rm Re}_m \approx c r_{\rm S}/\eta_{\rm max} = 10^3$ in the diffusion region. Note that the critical resistivity due to numerical diffusion in our code is much less, corresponding to $\eta_c = 10^{-5} c r_{\rm S}$. Hence, we find $\eta_{\rm max} = 100\eta_c$. The entropy of the gas can increase as a result of the dissipation of the magnetic energy and also the adiabatic compression in the shock.

We start calculations with a rotating torus in hydrostatic balance, which was calculated based on the assumption of a polytropic equation of state, $p = K\rho^{1+1/n}$ with $n = 3$, and a power-law specific angular momentum distribution, $l = l_0 (r/r_0)^a$ with $l_0 = (GMr_0^3)^{1/2}/(r_0 - r_{\rm S})$. Here $a$ and $r_0$ are parameters (assigned later). Then, the initial density and pressure distributions of the torus are explicitly written as

$$\rho_t(r,\phi,z) = \rho_0 \left(1 - \frac{\gamma}{v_{s,0}^2}\frac{\tilde{\psi} - \tilde{\psi}_0}{n+1}\right)^n \quad (6)$$

and

$$p_t(r,\phi,z) = \rho_0 \frac{v_{s,0}^2}{\gamma}\left[\frac{\rho_t(r,\phi,z)}{\rho_0}\right]^{1+1/n}, \quad (7)$$

where $\rho_0$, $v_{s,0}$, and $\tilde{\psi}$ denote, respectively, the initial density at $(r,z) = (r_0, 0)$, the sound velocity in the torus, and the effective potential given by

$$\tilde{\psi}(r,z) = \psi(r,z) + \frac{1}{2(1-a)}\left(\frac{l}{r}\right)^2. \quad (8)$$

In the present study we assign $a = 0.46$ and $r_0 = 40$ (in the unit of $r_{\rm S}$), where the Keplerian orbital time is $1124 r_{\rm S}/c$.

Outside the torus, we assume a nonrotating, spherical, and isothermal hot background (referred to as a background corona to distinguish from a disk corona created at later times as a result of magnetic activity within a flow) that is initially in hydrostatic equilibrium. This background corona asserts external pressure to magnetic jets. The density and pressure distribution of the background corona are

$$\rho_c(r,\phi,z) = \rho_1 \exp\left[-\frac{\psi(r,z) - \psi_1}{v_{s,c}^2/\gamma}\right] \quad (9)$$

and

$$p_c(r,\phi,z) = \rho_c(r,\phi,z) v_{s,c}^2/\gamma, \quad (10)$$

respectively, where $\rho_1$ and $\psi_1$ are density and potential at $(r,z) = (r_1, 0)$ with $r_1 = 2r_{\rm S}$ being the innermost radius, respectively, while $v_{s,c}$ is (constant) sound speed in the corona.

The initial magnetic fields are confined within a torus and purely poloidal. The initial field distribution is described in terms of the $\phi$-component of the vector potential, which is assumed to be proportional to the density, that is, $A_\phi \propto \rho$. (All other components are zero.) The strength of the magnetic field is represented by the plasma-$\beta$, the ratio of gas pressure to magnetic pressure, which is constant in the initial torus. Initial conditions are characterized by several nondimensional parameters, which are summarized in Tables 1 and 2. Here $E_{\rm th,0} \equiv v_{s,0}^2/\gamma|\psi_0|$ and $E_{{\rm th},c} \equiv v_{s,c}^2/\gamma|\psi_1|$, respectively, represent the ratios of thermal energy to gravitational energy in the initial torus and in the corona.

We impose the absorbing inner boundary condition at a sphere $R_1 = 2r_{\rm S}$. The deviation from the initial values of $\rho$, $p_{\rm gas}$, $\boldsymbol{v}$, and $\boldsymbol{B}$ is damped by a damping constant of

$$\mathcal{A} \equiv \frac{1 - \tanh\,[4(R - R_1)/\Delta R]}{2}, \quad (11)$$

where $\Delta R = 0.4 r_{\rm S}$ is a transition width. We calculate a corrected quantity $q^{\rm new}$ at each time step from an uncorrected quantity $q = q(r,\phi,z)$ by using the damping constant as

$$q^{\rm new} = q - (q - q^{\rm init})\mathcal{A}, \quad (12)$$

where $q^{\rm init}$ is the initial value.

We impose a symmetric boundary condition on the equatorial plane. On the symmetry axis ($z$-axis), $\rho$, $p_{\rm gas}$, $\boldsymbol{v}_z$, and $\boldsymbol{B}_z$ are set to be symmetric, while $\boldsymbol{v}_r$, $\boldsymbol{v}_\phi$, $\boldsymbol{B}_r$, and $\boldsymbol{B}_\phi$ are antisymmetric. The outer boundary conditions are free boundary conditions where all the matter, magnetic fields, and waves can transmit freely. Accordingly, not only outflow but also inflow from the outer boundary is permitted. For more details about the boundary conditions except the inner boundary, see Matsumoto et al. (1996).

Hereafter we normalize all the lengths, velocities, and density by the Schwarzschild radius, $r_{\rm S}$, the speed of light, $c$, and the initial torus density, $\rho_0 \equiv \rho(r_0, 0)$, respectively. Note that every term in each basic equation has the same dependence on density if we express field strength in terms of plasma-$\beta$, $B^2/8\pi = p_{\rm gas}/\beta$. Therefore, mass accretion rates can be taken arbitrarily, as long as radiative cooling is indeed negligible. This condition requires that accretion rates cannot exceed some limit, over which radiative cooling is essential (Ichimaru 1977; Narayan & Yi 1995).

The basic equations are solved by the three-dimensional MHD code based on the modified Lax-Wendroff scheme (Rubin & Burstein 1967) with the artificial viscosity (Richtmyer & Morton 1967, pp. 365–368). We use $200 \times 32 \times 200$ nonuniform mesh points. The grid spacing is uniform ($\Delta r = \Delta z = 0.16$) within the inner calculation box of $0 \leq r \leq 10$ and $0 \leq z \leq 10$, and it increases by 1.5% from one mesh to

TABLE 1
BASIC PARAMETERS

| Parameter | Definition | Adopted Values |
|---|---|---|
| Plasma-$\beta$ ..... | Gas pressure/magnetic pressure | 10 or 100 |
| $\rho_1/\rho_0$ ..... | Density at $(r_1, 0)$/density at $(r_0, 0)$ | $2.0 \times 10^{-5}$ |
| $E_{\rm th,0}$..... | $\equiv v_{s,0}^2/\gamma\|\psi_0\|$ | $1.45 \times 10^{-3}$ |
| $E_{{\rm th},c}$..... | $\equiv v_{s,c}^2/\gamma\|\psi_1\|$ | 1.0 or 0.1 |
| $v_{s,0}/c$..... | Sound velocity at $(r_0, 0)$ | $5.6 \times 10^{-3}$ |
| $v_{s,c}/c$..... | Sound velocity in corona | 0.91 or 0.65 |

TABLE 2
CALCULATED MODELS

| Model | Plasma-$\beta$ | $E_{\mathrm{th},z}$ | $v_{A,z}/c$ | $p_1/p_0$ [a] |
|---|---|---|---|---|
| A | 10 | 1.0 | 0.91 | 0.54 |
| B | 100 | 1.0 | 0.91 | 0.54 |
| C | 10 | 0.1 | 0.65 | 0.054 |
| D | 100 | 0.1 | 0.65 | 0.054 |

[a] $p_1$ is the pressure of background corona at $(r_1, 0)$.

the adjacent outer mesh outside this box up to $r \leq 20$ and $z \leq 20$, and it increases by 3% beyond that. The entire computational box size is $0 \leq r \leq 100$ and $0 \leq z \leq 100$. We simulate a full 360° domain (in comparison with HB02 and INA03, who solved only a 90° wedge).

## 3. MHD ACCRETION FLOW AND JET

### 3.1. *Emergence of a Magnetic Tower Jet*

We first display the overall evolution of model A in Figure 1, in which azimuthally averaged density contours with velocity vectors are shown for six representative time steps. Initially, a dense, geometrically thin disk is surrounded by a hot, tenuous

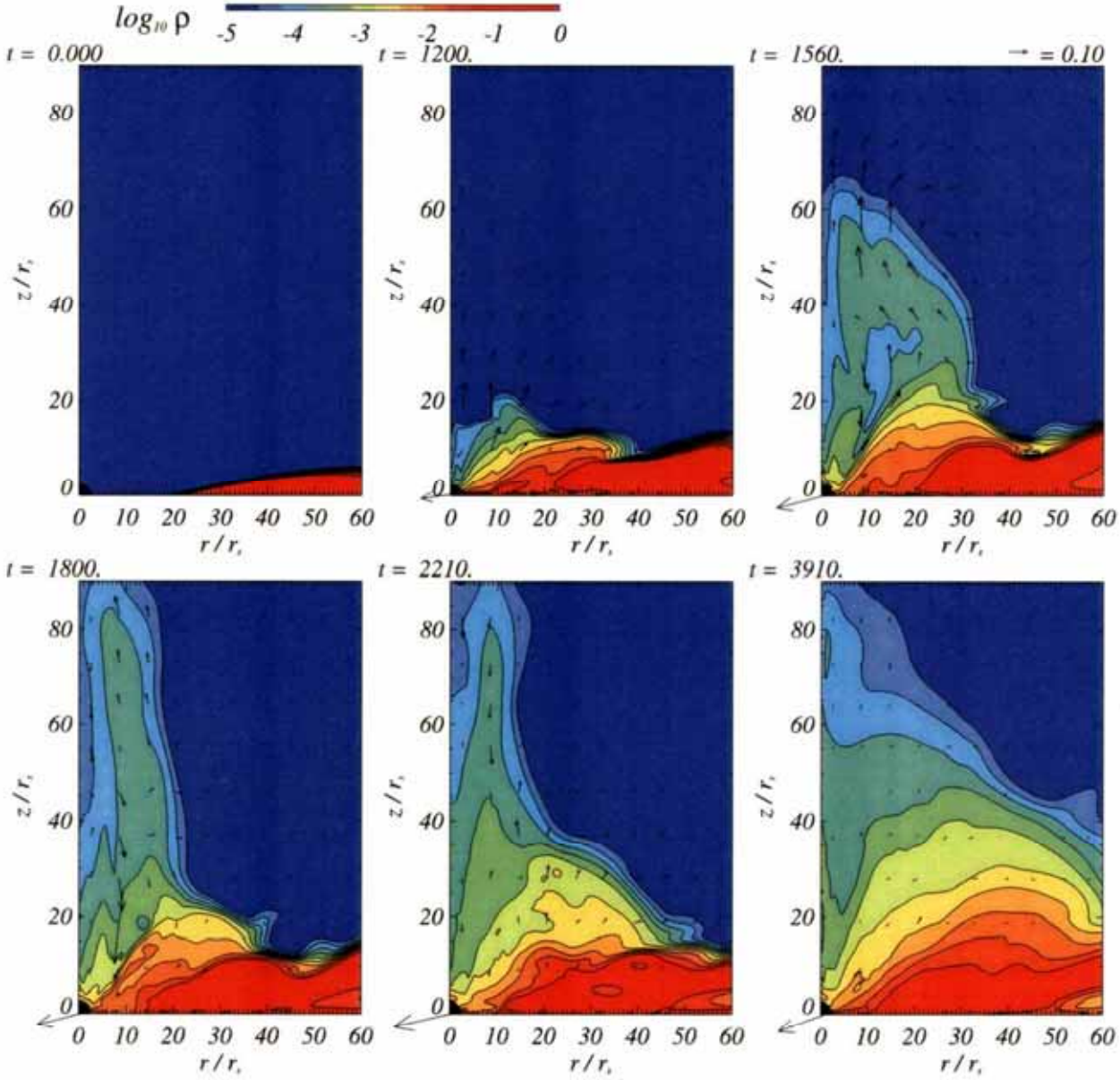


FIG. 1.—Time evolution of the density contours of model A with velocity vectors being overlaid. The density contours with colors are equally distributed on logarithmic scale with spacing being 0.4. The elapsed times are indicated in the upper left corner of each panel. The unit of time is $r_S/c = 10^{-4}(M/10\ M_\odot)$ s. A magnetic jet first grows at $t = 1000-1800$ but loses power at later times, producing more spherical density distribution.

background corona (see the upper left panel). When disk material reaches the innermost region close to the central BH, upward motion of gas is triggered (see the upper middle panel), which is driven by increased magnetic pressure of accumulated toroidal fields (shown later). Matter is blown away upward by inflating toroidal fields (a so-called magnetic tower) with a large speed, about several tenths of $c$ (see the upper right panel). Some fraction of matter then goes upward and leaves the displayed region (note that this figure shows only a part of our calculation box). Eventually, the magnetic tower stops vertical inflation and turns to shrink because of external pressure by the background corona (discussed later). Accordingly, part of the blown-up matter falls back toward the equatorial plane (see the lower left and lower middle panels). Finally, nearly quasi–steady state is realized, when a geometrically thick structure persists (see the lower right panel).

We can roughly divide the entire evolution of a rotating torus initially threaded by poloidal fields into two distinct phases: a transient, extended jet phase (hereafter phase I) and a subsequent quasi-steady phase (or phase II).

Figure 2 displays more detailed structure in phase I of model A. The left panel shows the contours of the plasma-$\beta$ on the logarithmic scale. We can easily distinguish jet regions, which have blue colors and thus are in low $\beta$, and ambient red regions, which are in high $\beta$. Most of the matter inside the jet is blown outward, although downward motion is also observed partly, especially near the rotation axis. Total pressure (a sum of gas pressure and magnetic pressure) decreases with an increase of height in nearly plane-parallel fashion, as is shown by the contours with black solid lines. It is interesting to note that total pressure inside the jet is nearly uniform in the horizontal direction at $z > 20$, indicating that the magnetic tower is balanced with the ambient gas pressure. Without external pressure by the background corona, a magnetic tower would expand along the directions of 60° tilted from the rotation axis (Lynden-Bell & Boily 1994). Model A shows that a magnetic tower evolves nearly in the vertical direction, which is made possible because of substantial external pressure (Lynden-Bell 1996).

The right panel of Figure 2 shows the contours of $B_\phi/B_p$. This figure is useful to check which of toroidal or poloidal fields are dominant in which region. We can immediately understand that the core of the jet has a blue color, implying poloidal components being more important, while the surrounding zone of the jet has an orange color, indicating dominant toroidal field components. Obviously, toroidal fields can be easily generated, as matter drifts inward, as a result of faster rotation and larger shear at smaller radii.

Such different field configurations near the surface and in the core of the jet are more artistically visualized in the three-dimensional fashion in Figure 3. Here thick red lines indicate magnetic field lines and thick green-to-blue lines represent streamlines with indication of velocities by the color; blue, green, and yellow represent velocities of ~0.1, 0.3, and 0.4 (in units of $c$), respectively. We can understand why magnetic field configuration of a sort that we encounter here is called "a magnetic tower." Volume inside the tower is mostly occupied by tightly wound toroidal fields. At the same time, we also observe vertical field lines in the core of the jet. As time goes on, this magnetic tower inflates vertically as a result of the growing magnetic pressure by the accumulated toroidal fields. Accordingly, the jet is also driven by enhanced magnetic pressure of the magnetic tower. Matter attains velocity up to $\sim 0.1c$–$0.2c$ at the top.

We have checked how much of a fraction of energy leaves the calculation box in which form (see Table 3). The values in the table are shown by the percentage of the sum of time-averaged fluxes listed in the column at each phase. Generally, the energy carried by jets does not dominate the total energy loss from the system. In model A, for example, the outflow energy is only ~0.5% of the total energy loss.

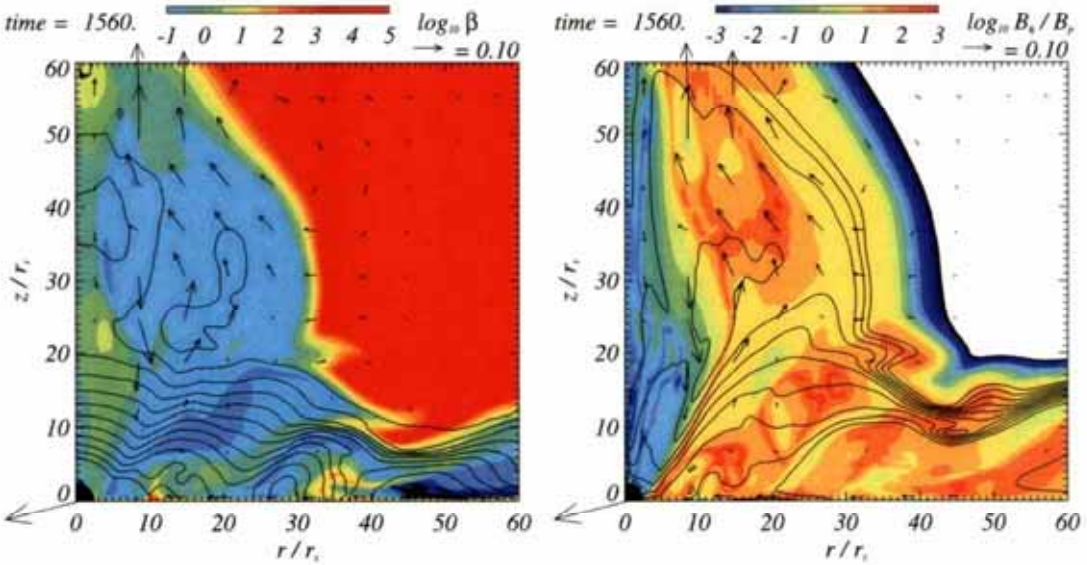


FIG. 2.—Color contours of plasma-$\beta$ (*left*) and magnetic pitch (*right*) in phase I of model A, overlaid with velocity vectors and total pressure (*left*) and density (*right*) contours with black solid lines in logarithmic scale. Contour level of total pressure is $P_{\rm tot}(N) = -6.0 + 0.15N$, where $N$ is an integer from 0 to 14, while that of density is the same as in Fig. 1.

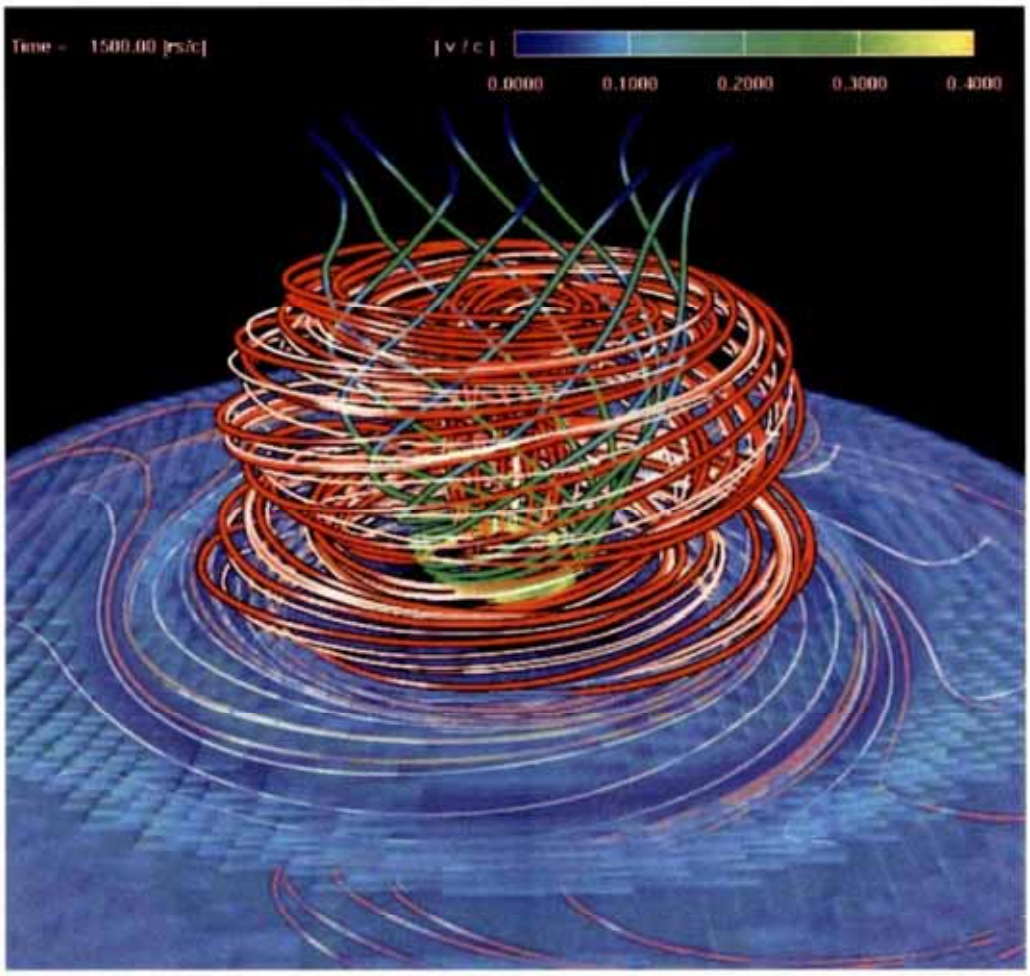


FIG. 3.—Perspective view of magnetic field lines in phase I of model A. Thick red (or thin white) lines indicate magnetic field lines that are anchored to the innermost (somewhat outer) zones at $(r, z) = (1, 1.5)$ $[(r, z) = (56, 10)]$. Thick green lines denote the streamlines of velocity vectors integrated from $(r, z) = (8.5, 7)$, whereas the color bar indicates the velocity. The light-blue shaded region indicates the isovolume of the density ($\rho = 0.025\rho_0$). Accumulated toroidal fields emerging from the disk produce a magnetic tower, thereby driving an MHD jet. Jet material is surrounded by toroidal magnetic fields, whereas poloidal (vertical) fields dominate inside the jet.

TABLE 3

FRACTION OF FLUX

| Flow | Flux[a] | A/I (%) | A/II (%) | B (%) | C (%) | D (%) |
|---|---|---|---|---|---|---|
| Outflow | $c\langle \boldsymbol{E} \times \boldsymbol{B} \rangle_z$[b]$/4\pi$ | 0.13 | 0.00 | 0.00 | 3.14 | 0.53 |
| | $\langle (\rho v^2/2) \mathbf{v}_z \rangle$ | 0.14 | 0.00 | 0.00 | 8.99 | 0.69 |
| | $\langle \gamma p/(\gamma - 1) \mathbf{v}_z \rangle$ | 0.27 | 0.00 | 0.00 | 1.21 | 0.21 |
| Inflow | $c\langle \boldsymbol{E} \times \boldsymbol{B} \rangle_{\rm in}$[c]$/4\pi$ | 0.03 | 0.03 | 0.05 | 1.0 | 0.22 |
| | $\langle (\rho v^2/2) \mathbf{v}_{\rm in} \rangle$ | 29.11 | 29.25 | 28.34 | 28.29 | 28.19 |
| | $\langle \gamma p/(\gamma - 1) \mathbf{v}_{\rm in} \rangle$ | 30.99 | 31.13 | 30.15 | 34.94 | 30.20 |
| | $\langle \rho w \mathbf{v}_{\rm in} \rangle$ | 39.42 | 39.60 | 41.45 | 24.96 | 40.40 |

[a] The energy and enthalpy flux passing through $z = 50$ is azimuthally averaged and is integrated over $5 \le r \le 30$, while that of the inflow is integrated inside the sphere $R = 2.2$.

[b] The subscript $z$ indicates the vertical ($z$) component of a vector.

[c] The subscript "in" indicates the $\boldsymbol{e}_{\rm in}$ component of a vector where $\boldsymbol{e}_{\rm in} = -(\boldsymbol{e}_r \cos\theta + \boldsymbol{e}_z \sin\theta)$ is a unit vector, $\sin\theta/\cos\theta = z/r$, and $\boldsymbol{e}_r$ is the radial ($r$) component of a unit vector.

### 3.2. *Quasi-steady MHD Flow*

Eventually the initial jet loses its power, and the system enters a quiet, quasi–steady state. First, we show in Figure 4 the radial distributions of representative physical quantities in both phase I (*thick solid lines*) and phase II (*thick dashed lines*). The adopted quantities are density, radial velocity, pressure, specific angular momentum, sound velocity, and mass accretion rate, $\dot{M} \equiv -\int_0^{H} 2\pi r \rho v_r \, dz$ with $H = 1.0$ being fixed. These quantities are azimuthally and vertically averaged over $0 \le \phi \le 2\pi, 0 \le z \le 1$, except the mass accretion rate, which is a vertical integral.

Roughly speaking, these quantities show power-law relations, i.e., $\rho \propto r$ at small radii, while $\rho \propto r^{-1}$ at large radii, $v_r \propto r^{-1/2}$ except at the inner outflowing part, $l$(specific angular momentum) $\propto r^{0.5}$, meaning a nearly Keplerian rotation, $c_s$(sound velocity) $\propto r^{-1/2}$, and $\dot{M} \sim$ const in space in the inner region. All of these relations resemble closely those of the previous work (i.e., Stone & Pringle 2001; HB02). Note that our results are consistent with a hot, thick, near-Keplerian disk and a subthermal magnetic field. The density distribution is inconsistent with ADAF models, since ADAF shows a steeper density profile, approximately $\rho \propto r^{-3/2}$.

The most interesting feature in the present simulations is found in Figure 5, which illustrates contours of the total pressure (*black solid lines*) and plasma-$\beta$ (*color contours*) in the left panel and those of density (*black solid lines*) and $B_\phi/B_p$ (*color contours*) in the right panel in phase II of model A calculations. We find that the total pressure distribution is not plane-parallel and the plasma-$\beta$ distribution has inhomogeneous structure around the central BH.

Interestingly, high-$\beta$ ($\sim$100) plasmas (indicated by orange color in the left panel) distributed in the radially extended zone, which is tilted by $\sim$30° from the $z$-axis (in the perpendicular direction to the isopressure contours), are sandwiched by moderately low $\beta$ ($<$1) plasmas (indicated by blue color). There is another high-$\beta$ region extending from point $(r, z) \sim (15, 0)$ to the upper left region. We also notice that poloidal (or toroidal) fields are dominant in these high-$\beta$ (low-$\beta$) regions, as is indicated by orange (green or blue) colors in the right panel. As a consequence, mass accretion onto the central BH

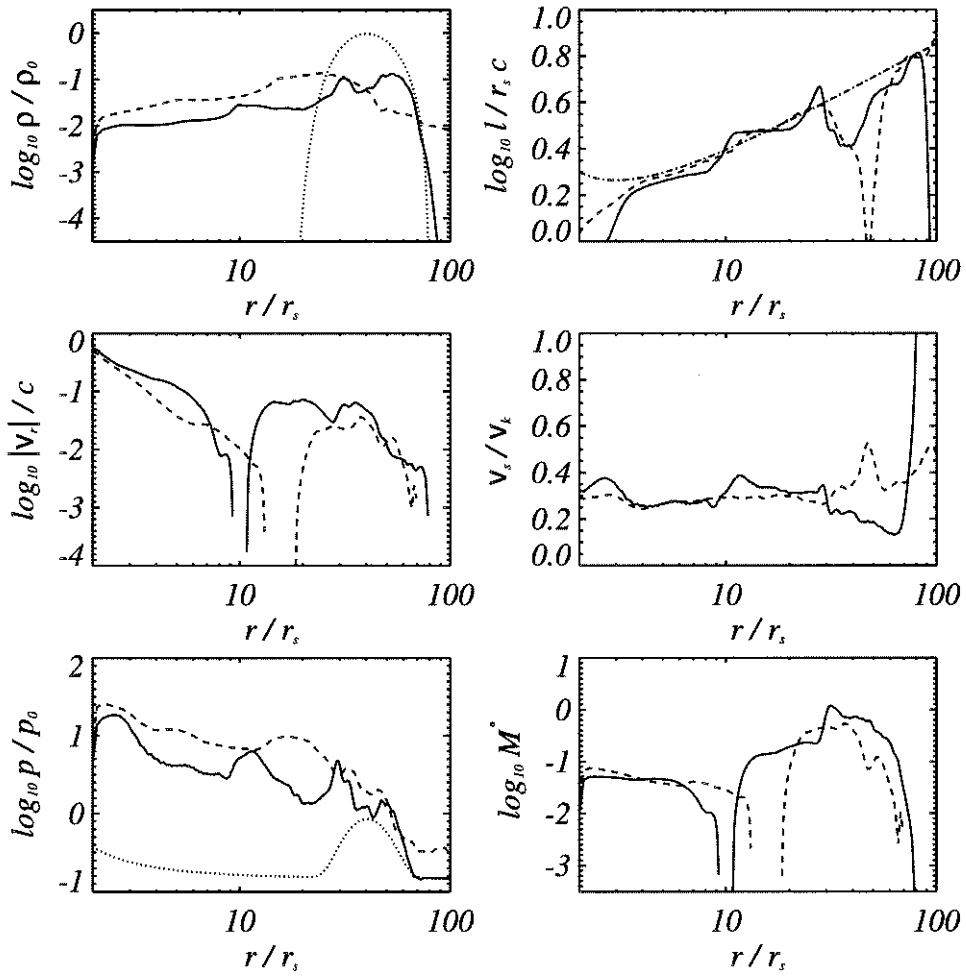


FIG. 4.—Radial structure of the flow of model A on the equatorial plane in phase I ($t = 1560 r_S/c$; transient extended jet phase; *solid curves*) and phase II ($t = 3910 r_S/c$; subsequent quasi-steady phase; *dashed curves*). From the top left to the bottom right, density, radial velocity, pressure, specific angular momentum, sound velocity, and mass accretion rate are plotted. The dotted lines indicate initial conditions for density and pressure, while a dot-dashed line indicates a Keplerian specific angular momentum.

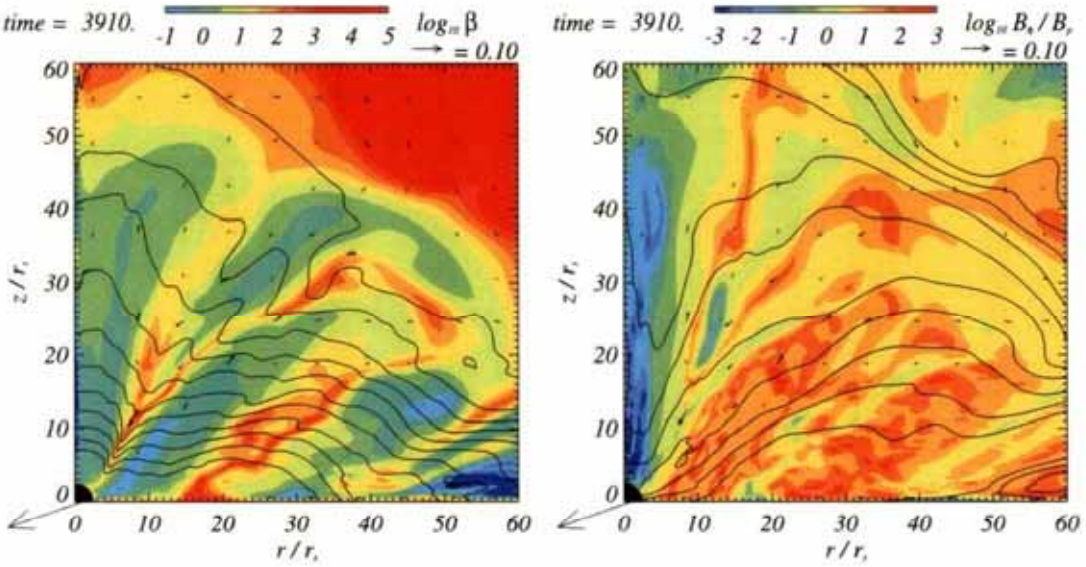


FIG. 5.—Same as Fig. 2, but in phase II of model A

takes place mainly through the equatorial plane at $r < 20$. We also notice that poloidal (vertical) fields are still evident along the rotation axis, along which downward motion of gas is observed.

We find that equi-$\beta$ contours slightly change with time. The accretion flow is inherently time dependent, as it is driven by MHD turbulence. There are two possibilities for the origin of time dependence in this case. One is the axisymmetric mode of MRI (so-called channeling mode). Since the structure of quasi-steady flow is nearly axisymmetric, the channeling mode of MRI can grow in our simulations. As a result, high-$\beta$ plasma is created between the low-$\beta$ plasmas with opposite directions of the flow. Another possibility is magnetic buoyancy. If we assume pressure balance among neighboring high- and low-$\beta$ regions, matter density should be high in the former, since magnetic pressure is less in the former. This gives rise to magnetic buoyancy for the latter, inducing its rising motion in the direction opposite to that of gravity. Such a rising magnetic loop was simulated by Turner et al. (1999), who found that the rising loop evolves into a jet (see also KMS02 for global simulations). In both cases, magnetic reconnection can be triggered. We find that the directions of toroidal fields are antiparallel across the high-$\beta$ region. Thus, magnetic reconnection can take place in this high-$\beta$ region and high-velocity plasmoid can be ejected from this site. If this is the case, the high-$\beta$ region may move outward. Velocity vectors plotted in this figure show both outward and inward motions, although their absolute values are small. The situation is rather complex. To make clear what is happening in the quasi–steady state, we need more careful studies.

It will be highly curious to see how magnetic field configuration changes after the jet eruptions. In Figure 6 we plot the perspective view of the magnetic field lines and matter trajectories in phase II of model A. Field-line configurations are distinct from those in phase I. Field lines that are connected to the innermost part of the flow (indicated by red thick lines) now show much simpler structure than in phase I and are dominated by the poloidal component, implying that toroidal fields found in phase I have already been blown away. Note, however, that the surrounding region is still dominated by toroidal fields, as are indicated by white thick lines. As a consequence, the magnetic tower is not clearly seen.

In order to see more clearly how toroidal and poloidal fields are generated and accumulated with time in the disk and the corona, we plot the strength of each component as a function of radius at several time steps in Figure 7. Toroidal fields increase in strength by the shear and dominate in the entire region (at $t = 1200$), but they are blown away from the disk by the emergence of a jet and thus decrease in strength (at $t = 1560$), whereas poloidal fields are generated as a result of the emergence of the magnetic tower from the disk. After the substantial ejection of matter and toroidal fields, the axial part of the corona $r < 7$ is dominated by poloidal fields. Toroidal fields can be blown off with jet material, but poloidal fields created by vertical inflation of toroidal fields should remain. Note that, since no continuous injection of mass and fields is assumed in our calculation, the increase of the poloidal fields in the inner zone is eventually saturated. If we would add more fields, they would continuously grow.

We finally plot the energetics of model A in Figure 8. Kinetic energy always dominates others in both phases; that is, magnetic fields are not strong enough to suppress accreting motion of the gas. There is no evidence of huge buildup of net field that would inhibit accretion onto the central BH in our simulations, unlike the picture obtained by INA03.

### 3.3. *Cases of Weak Initial Fields and/or Low External Pressure*

Before closing this section, let us see some parameter dependence of our results. In models B–D, we vary the initial magnetic field strengths and/or external pressure by the background corona. To help in understanding different conditions, we plot the initial radial distribution of pressure (gas and magnetic) in Figure 9 for each model. We see that external pressure is comparable to initial torus pressure in models A and B, while the external pressure is totally negligible in models C and D.

The later evolution is shown in Figure 10. First, the case of initially weaker magnetic fields (model B) is displayed in the

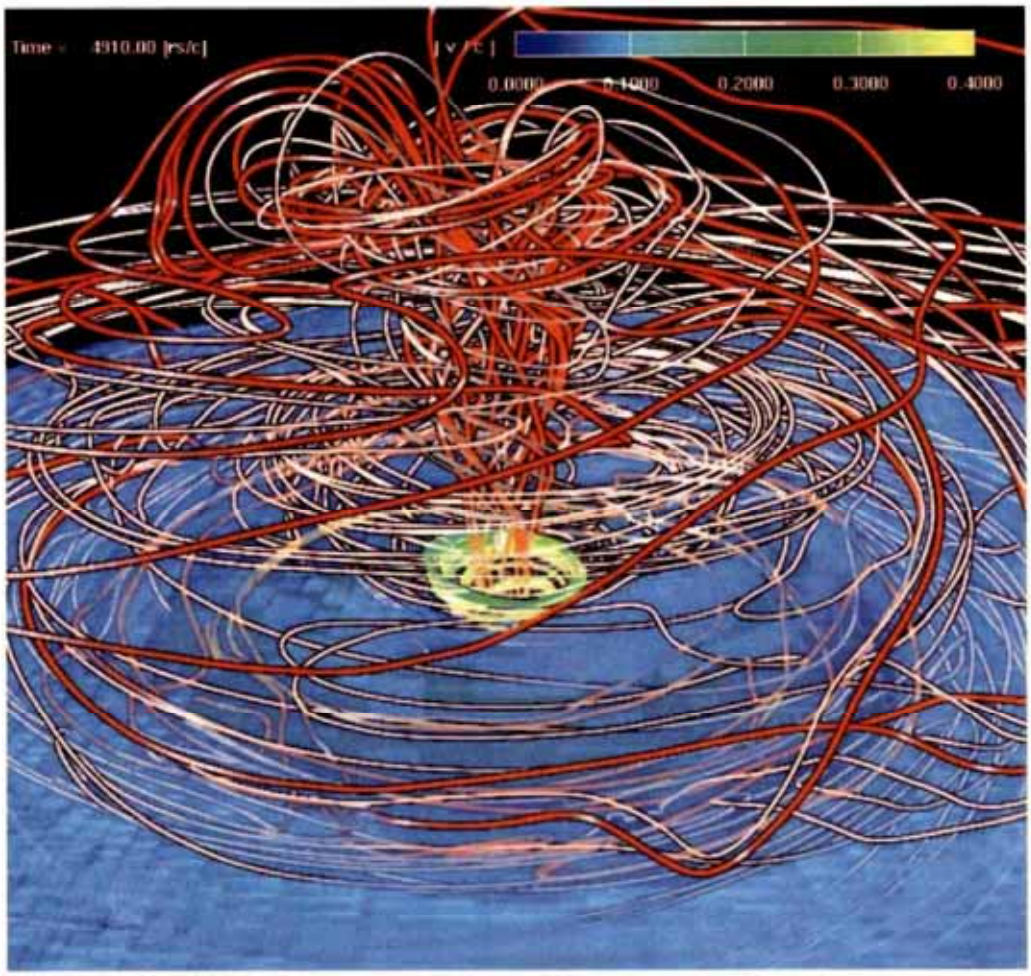


FIG. 6.—Same as Fig. 3, but in phase II of model A. Magnetic field lines represented by thick red lines are more confined, compared with those in Fig. 3. Thin white lines (representing the fields lines emerging from somewhat outer zones) look similar to those in Fig. 3. Thick green lines indicating the streamlines of velocity vectors only appear near the BH and are not evident.

second row of Figure 10. Importantly, we do not see a strong outflow. The absence of an obvious jet can be understood in terms of pressure balance. Since magnetic field strength is by 1 order of magnitude smaller in model B than that in model A, the initial magnetic pressure is much smaller than external pressure (see Fig. 9). Magnetic pressure can grow as the disk dynamo works, but magnetic pressure is not yet large enough to overcome external pressure at the moment that the disk material reaches the innermost region. Note that the time needed for the torus material to reach the center is much longer in model B than in model A because it takes a longer time for fields to be strong enough to promote rapid accretion. Since the magnetic pressure inside the disk is comparable to the background pressure in model A initially, it is easy to overcome the background pressure. Hence, eruption of a magnetic jet is possible. Nevertheless, it is interesting to note that the subsequent states look similar among models A and B. This indicates that phase II structure is not sensitive to the strengths of initial magnetic fields, although it is not yet clear that the results may or may not depend on the initial magnetic field orientations.

The cases of weaker external pressure (models C and D) are illustrated in the third and fourth rows of Figure 10. We find stronger, wider, and longer standing (nearly persistent) jets in these models. This demonstrates that the duration of a jet and its width are sensitive to how large external pressure is. Again, the flow structure in phase II looks similar among models C and D, but unlike cases with stronger external pressure (models A and B) there is a conical low-density region present near the symmetric ($z$) axis. This is due to the ejection of mass from the innermost part via jets.

We find in Table 3 that the total energy output by the jet amounts to $\sim$10% of the total energy loss at maximum in model C (with strong initial magnetic field and low external pressure). Except for this model, total energy output is negligible. How much of a fraction of energy can be carried away from the BH system thus depends critically on external pressure and field strength, and it is not always possible to achieve a high efficiency of energy extraction by jets.

Finally, we summarize our simulation results in the schematic picture (see Fig. 11). In Figure 11, high-$\beta$ plasma with highly turbulent motion is located at the equatorial plane. Magnetic field generated by the dynamo action taking place inside the disk emerges upward and creates the disk corona with intermediate-$\beta$ plasma. In the inner region of the disk, the

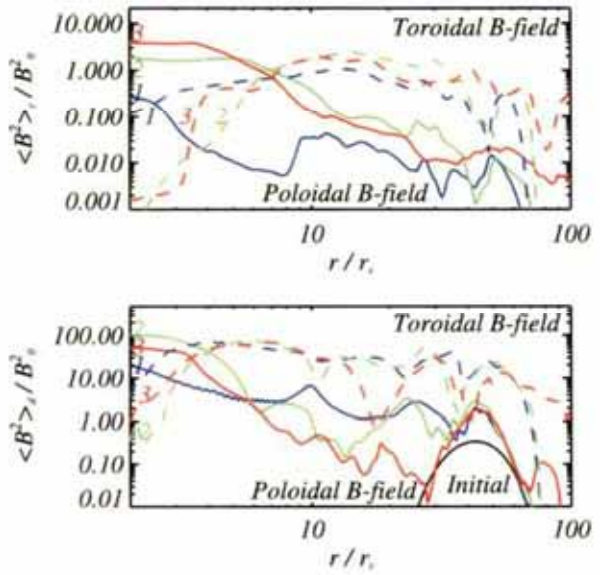


FIG. 7.—Changes of the magnetic energy density in the disk (*bottom*) and in the corona (*top*) from their initial values as functions of radius for model A. Each panel presents the magnetic energy density of poloidal (*solid lines*) and that of toroidal fields (*dashed lines*). The magnetic energy in the disk (or in the corona) is integrated from $z = 0$ to 5 (from $z = 5$ to 100). The elapsed times are 1200, 1560, and 3910 (in $r_S/c$), corresponding to the labels 1, 2, and 3, respectively.

emerging magnetic field erupts into the external corona and deforms into the shape of the magnetic tower. Such a magnetic tower ejects disk material upward by its magnetic pressure and creates the magnetic tower jet. The magnetic tower jet collimates at the radius where the magnetic pressure of the tower is balanced with the external pressure.

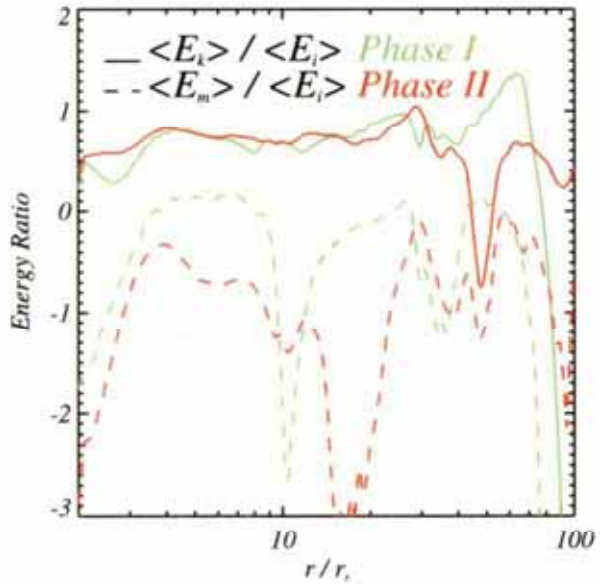


FIG. 8.—Energetics of model A. The ratio of kinetic energy ($E_k$) to thermal energy ($E_i$) and the ratio of magnetic energy ($E_{mag}$) to thermal energy ($E_i$) are plotted as functions of radius in phases I ($t = 1560 r_S/c$) and II ($t = 3910 r_S/c$), respectively. Kinetic energy always dominates over others by about 1 order of magnitude.

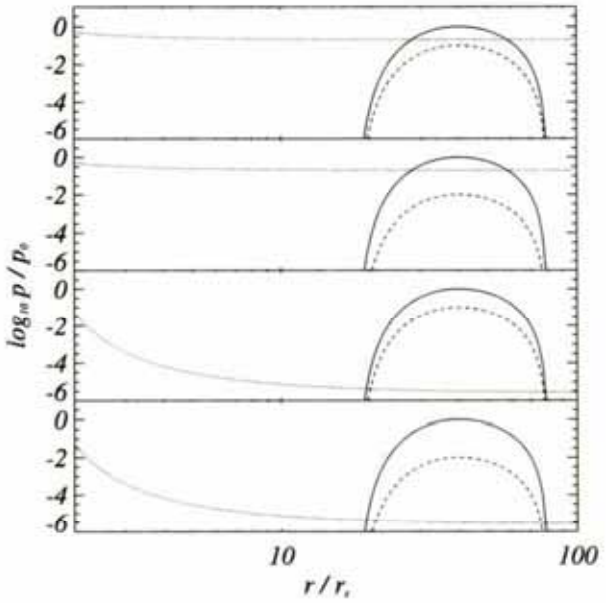


FIG. 9.—Initial pressure distributions for models A, B, C, and D (*top to bottom*). The solid and dashed lines represent the gas and magnetic pressures at $z = 0$, respectively, while the dotted lines represent external pressures by the background corona extrapolated to the $r$-axis ($z = 0$; see eq. [10]). All values are normalized by the pressure at the density maximum of the torus $(r, z) = (r_0, 0)$.

## 4. DISCUSSION

### 4.1. *Brief Summary*

We performed three-dimensional MHD simulations of the radiatively inefficient rotating accretion flow around BHs. We examined the case with initially poloidal field configurations with $\beta = 10$ and 100. When the bulk of torus material reaches the innermost region close to the central BH, a magnetic jet is driven by magnetic pressure asserted by accumulated toroidal fields (magnetic tower). The fields are mostly toroidal in the surface regions of the jets, whereas poloidal (vertical) fields dominate in the inner core of the jet. The collimation width of the magnetic jet depends on external pressure; the more enhanced the external pressure is, the more collimated the jet is. Nonnegligible external pressure tends to suppress the emergence of the MHD jets.

The jet outflow is, however, a transient phenomenon, unless the external pressure is negligible. After several dynamical timescales at the radius of the initial torus, the jet region shrinks and the flow structure completely changes. After the change, the flow is quasi-steady and possesses complex field configurations.

The nature of the quasi–steady state differs from that of INA03. We have seen that poloidal fields are dominant near the $z$-axis and that the BH is mostly surrounded by marginally low $\beta$ plasma with toroidal fields being dominant. This view is different from that simulated by INA03, who found a magnetosphere composed of significantly low $\beta$ ($\sim 10^{-3}$) plasmas with poloidal fields and that mass is not allowed to directly pass into the magnetosphere. Instead, mass accretion occurs along the radial narrow streams with slow rotation. We discuss in § 4.3 what the origin of difference would be.

### 4.2. *Magnetic Tower Jet*

The acceleration mechanism of the MHD jet, starting with a disk threaded with large-scale, external vertical fields, has been

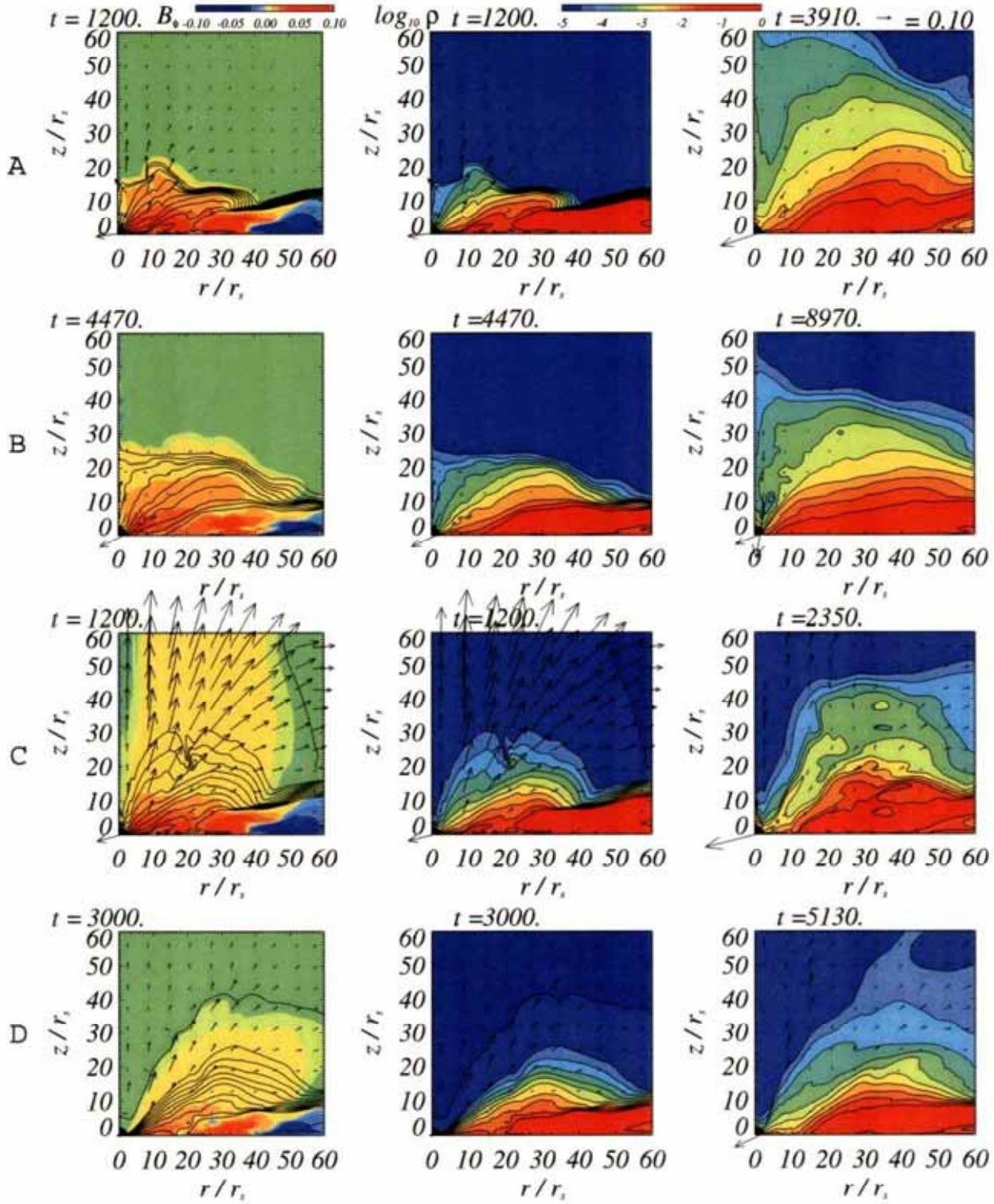


FIG. 10.—Summary of the results of four calculated models. From left to right, contours of toroidal field strengths and of density in different times are displayed for models A, B, C, and D (*top to bottom*). Arrows show the velocity vectors. Initial magnetic field strengths are weaker in models B and D (in which $\beta = 100$ while $\beta = 10$ otherwise), while external pressure is 10 times weaker in models C and D.

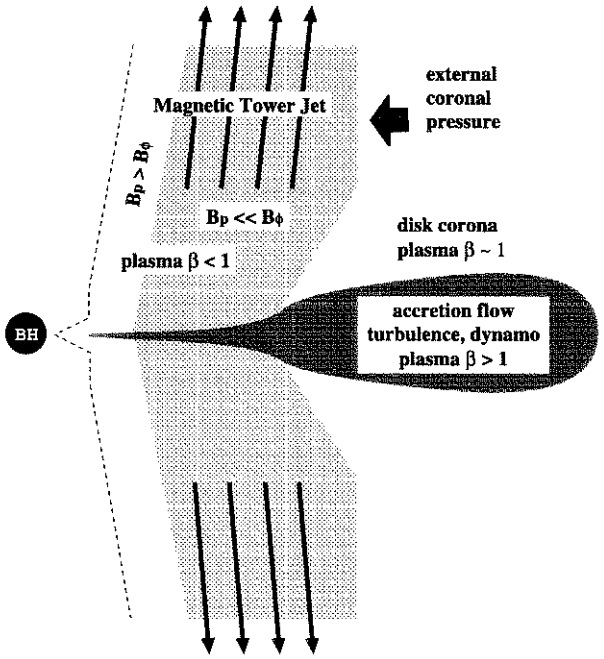


FIG. 11.—Schematics of the magnetic tower jets

studied extensively by many groups. It has been discussed that in the magnetocentrifugally driven jet, the poloidal magnetic field is much stronger than the toroidal magnetic field in the surface layer of the disk or in the disk corona, where plasma-$\beta$ is low (e.g., Blandford & Payne 1982; Pudritz & Norman 1986; Lovelace, Wang, & Sulkanen 1987). In this case, magnetized plasma corotates with the disk until the Alfvén point, beyond which the toroidal field starts to be dominated and hence collimation begins by its magnetic pinch effect. The Blandford-Payne (1982) mechanism can be applied to this kind of jet for determining the launching point of the jet.

On the other hand, there is another kind of magnetically driven jet, in which the toroidal magnetic field is dominated everywhere (e.g., Shibata & Uchida 1985; Shibata, Tajima, & Matsumoto 1990; Fukue 1990; Fukue, Shibata, & Okada 1991; Contopoulos 1995). In this case, the Alfvén point is embedded in the disk or there is no Alfvén point, and the collimation due to toroidal field begins from the starting point of the jet. The Blandford-Payne mechanism cannot be applied to such a jet.

The situation is similar if magnetic loops are anchored to the surface of the differentially rotating disk or that of the central object. The MHD jet generated from the weak, localized poloidal field in the disk (Turner et al. 1999; KMS02) belongs to the toroidal field–dominated jet. Moreover, the MHD jet generated from the dipole magnetic field is simulated by Kato, Hayashi, & Matsumoto (2004). They calculated time evolution of a magnetic tower jet, which is an extension of the Lynden-Bell (1996) magnetic tower and is also the toroidal field–dominated jet.

Our magnetic tower jet is also consistent with the toroidal field–dominated jet, since the magnetic tower is made of the toroidal field generated by dynamo action within the disk. It has often been argued that such a toroidal field–dominated jet is very unstable for kink instability in real three-dimensional space and cannot survive in actual situations (e.g., Spruit, Foglizzo, & Stehle 1997). However, our three-dimensional simulations showed, for the first time, that such a toroidal field–dominated jet survives at least for a few orbital periods of the disk and hence can be one of the promising models for astrophysical jets.

By means of the magnetic tower jets, one may ask what the condition for the formation of the toroidal field–dominated jet is. The formation of magnetic jets demands that the maximum magnetic pressure $p_{\rm mag}^{\rm max}$ generated within the disk must exceed the external pressure $p_{\rm ext}$. Since the growth of toroidal fields due to MRI is saturated under a certain value (e.g., $\beta_{\rm min} \sim 100$ within the disk; see Matsumoto 1999; Hawley 2000; INA03), we have a condition for the formation of the jet as follows:

$$p_{\rm mag}^{\rm max} = p_{\rm disk}/\beta_{\rm min} > p_{\rm ext}, \tag{13}$$

where $p_{\rm disk}$ is the pressure of the disk. Our conclusion is equivalent to that of KMS02 for the case of the isothermal background corona, in which they argued that if the coronal density is very high, it prevents the ejection of the magnetic loop.

If external pressure is very small, compared with initial torus (magnetic) pressure, magnetic fields can more easily escape from the disk than otherwise. The result is a strong, long-persistent jet, as we saw in models C and D. Although the collimation is not clear in the plot with limited box, collimation does occur but at large radii ($>60r_S$) in these models, since as the outflow expands, magnetic pressure decreases and eventually becomes comparable to the external pressure. We thus call it a jet, not a big wind, and the width of the jet depends on the external pressure.

If external pressure is very large and by far exceeds the maximum magnetic pressure inside the disk, conversely, the emergence of magnetic fields out of a disk is totally inhibited, which is the situation corresponding to model B. There will be no jets. Only when external pressure is mildly strong, comparable to the maximum magnetic pressure, can we have a transient eruption of a collimated magnetic jet (see model A).

It is important to note, in this respect, the works by Lynden-Bell. Lynden-Bell & Boily (1994) studied self-similar solutions of force-free helical field configurations, finding that such configurations expand along a direction of 60° away from the axis of the helical field. The modified model by Lynden-Bell (1996) asserts that a magnetic tower can be confined by external pressure. Here, by three-dimensional MHD simulation, we successfully show the formation process of the magnetic tower, which is stable for a few dynamical timescales at the density maximum of the initial torus. Our three-dimensional magnetic tower solution is basically the same as the one he proposed.

Unfortunately, there were not always detailed descriptions regarding external pressure given in previous MHD simulation papers, although the presence of external pressure is indispensable to perform long-term simulations. INA03 claimed that even with continuous supply of mass and fields, the bipolar jet (or outflow) phase is transient. Their case seems to correspond to the case with relatively strong external pressure (i.e., our model A). If this is the case in actual situations, we expect strong jets only when a burst of large accretion flow takes place. This may account for the observations of a microquasar, GRS 1915+105, which recorded big (superluminal) jets always after sudden brightening of the system (Klein-Wolt et al. 2002).

It is interesting to discuss the collimation mechanisms of the jet. We checked the force balance, confirming that it is external pressure that is balanced with magnetic pressure at the boundary between the jet and the ambient corona. Together with our finding that jet widths depend also on the value of external pressure, we are led to the conclusion that for jet collimation, external pressure plays important roles in the present case.

Furthermore, the total pressure of the magnetically dominated "corona," created above the disk as a result of the eruption of the magnetic tower jet in early phase, could be greater than that of the background pressure (hereafter we call it the "disk corona" in order to distinguish it from the background corona; see also two-layered structure of accretion flow as presented by HB02). Thus, we expect that the collimation widths of a successive jet would be smaller than that in the case of model A.

To sum up, we demonstrate the important role of external pressure asserted by ambient coronal regions on the emergence, evolution, and structure of a magnetically driven jet. We need to remark how feasible the existence of a nonnegligible external pressure is in realistic situations. Fortunately, we have a good reason to believe that ambient space of the accretion flow system may not be empty. If there is magnetic dynamo activity in the flow, magnetic fields will be amplified and eventually escape from the flow, forming a magnetically confined corona (Galeev, Rosner, & Vaiana 1979). Then, mass can be supplied from the flow to a corona via conduction heating of the flow material. In fact, the density of the disk corona is basically explained by the energy balance between conduction heating and evaporation cooling of the disk chromosphere (Liu, Mineshige, & Shibata 2002). Thus, it is reasonable to assume that ambient space surrounding a magnetized flow is full with hot tenuous plasmas as a result of previous magnetic activity of the disk and that the hot corona is exerting external pressure on the flow with comparable magnitude.

Finally, we remark on the comparison with the simulations by HB02. They also calculated the evolution of a torus threaded with poloidal fields, adopting similar initial conditions as we did. But there is a distinction: we find a significantly low $\beta$ jet, whereas HB02 obtained a high-$\beta$ jet (see their Fig. 1).

In contrast to HB02, our jet is driven by the magnetic pressure inside the magnetic tower. Although we found the outflow along the funnel barrier inside the core of the magnetic tower in models C and D (Fig. 10), the outflow is not driven by the gas pressure but by the magnetic pressure. Furthermore, we note that averaged plasma-$\beta$ along the funnel barrier where the poloidal field dominates the toroidal field is of the order of unity (Fig. 5). In comparison with HB02, the discrepancy can be explained by the difference of external pressure. For instance, in models C and D, there are persistent jets that look like uncollimated winds reported in HB02. This is because the external pressure was too low to confine the magnetic tower inside the computational box.

### 4.3. *Steady State Picture of MHD Accretion Flow*

The flow structures in the quasi-steady phase that we obtained in our simulations look similar to those of previous work except INA03. There is a big distinction: INA03 claimed the formation of a significantly low $\beta$ (with $\beta \sim 10^{-3}$) magnetosphere dominated by a dipolar magnetic field. Since any motion passing through the magnetosphere is inhibited, accretion occurs mainly via narrow slowly rotating radial streams. We, in contrast, find the formation of a $\beta \sim 1$ region (on average) that is dominated by toroidal magnetic fields, although the structure is quite inhomogeneous and is a mixture of high- and low-$\beta$ zones. Importantly, the fields are not too strong to inhibit gas accretion, since magnetic field strength is amplified by the dynamo action inside the disk as a result of MRI and the spatially averaged plasma-$\beta$ inside the disk is unlikely to become less than unity in general. Mass accretion occurs predominantly along the equatorial plane. Mass inflow toward the BH from the other directions is also found, but mass flow rates are not large because of smaller density than the value on the equatorial plane.

We can easily demonstrate that it is not easy to create an extended magnetosphere that has significantly low $\beta$-values. Suppose that magnetic fields are completely frozen into material. As a gas cloud contracts, it gets compressed as a result of geometrical focusing. If the gas cloud shrinks in nearly a spherically symmetric way, the density and gas pressure increase as $\rho \propto r^{-3}$ and $p \propto \rho^{\gamma} \propto r^{-5}$ for $\gamma = \frac{5}{3}$, respectively, in radiatively inefficient regimes. Because of the frozen-in condition, poloidal fields are also amplified according to the relation $B_z \propto r^{-2}$, as long as the total magnetic flux, $B_z\, r^2$, is conserved; that is, magnetic pressure also increases but more slowly, $p_{\rm mag} > B_z^2/8\pi \propto r^{-4}$. Thus, the plasma-$\beta$ should *increase* as the gas cloud contracts, as $\beta \equiv p_{\rm gas}/p_{\rm mag} \propto r^{-1}$. Regions just above and below the BH (in the vertical direction) can have low-$\beta$ plasmas, since matter can slide down to the BH along the vertical fields, but it is unlikely that low-$\beta$ regions can occupy a large volume.

If the gas cloud shrinks in the two-dimensional fashion, conversely, the plasma-$\beta$ will decrease as the gas cloud contracts, since then gas density is proportional to $\rho \propto r^{-2}$, thus yielding $p_{\rm gas} \propto r^{-2\gamma} \propto r^{-10/3}$ (for $\gamma = \frac{5}{3}$) and $\beta \propto r^{2/3}$. This is not the case in our simulations, which show that matter is more concentrated around the equatorial plane.

It might be noted that the surface of a magnetosphere may be unstable against the magnetic buoyancy instabilities such as interchange instability (so-called magnetic Rayleigh-Tayer instability; Kruskal & Schwarzschild 1954) and undular instability (so-called Parker instability; Parker 1966), since heavy materials are located above field lines with respect to the direction of gravity. Roughly speaking, the critical wavelength, over which perturbation is unstable against the Parker instability, is $\lambda_c \sim 4\beta^{-1/2}H$ (with $H$ being the pressure scale height; see Matsumoto et al. 1988). When $\beta \sim 10^{-3}$, we have $\lambda_c \sim 100H > r$, since $H/r$ cannot be as small as $H/r \sim 10^{-2}$. The Parker instability is completely stabilized under such circumstances, but interchange instability can occur (e.g., Wang & Nepveu 1983). In our case with a relatively large $\beta \sim 1$, on the other hand, there are frequent chances to trigger the Parker instability. The growth timescale of the Parker instability is $(2\text{–}4)H/v_{\rm A}$. As a result, heavy gas easily sinks down through a moderately magnetized region.

We need to note again that kinetic energy (including orbital energy) always dominates over magnetic and thermal energy, meaning that there is no sign of huge magnetic fields inhibiting accretion as INA03 claimed. It is not clear if magnetic buoyancy instability helps accreting motion of gas. Further, we should note that anomalous resistivity always turns on near the BH, meaning the effective occurrence of magnetic reconnection. In any case, our picture of the quasi-steady phase of MHD accretion flow is that matter can accrete onto a BH on relatively short timescales.

We studied the case of initially poloidal fields. A natural question is how universal our conclusion is. The simulations starting with toroidal fields (INA03; Machida & Matsumoto 2003) show no strong indication of magnetic jets. This is a big difference. However, toroidal fields can be more easily created by differential rotation than poloidal fields. We thus find that toroidal fields can suddenly grow and dominate over poloidal fields in a large volume (see Fig. 7). We can expect similar quasi–steady state, even if we start calculations with toroidal fields. To this extent, our study is consistent with those of initially toroidal field with low external pressure. The comparison is left as future work.

Numerical computations were carried out on VPP5000 at the Astronomical Data Analysis Center of the National Astronomical Observatory, Japan (yyk27b). This work was supported in part by the grants-in-aid of the Ministry of Education, Science, Sports, Technology, and Culture of Japan (13640328, 14079205, S. M.).

REFERENCES

Balbus, S. A. 2003, ARA&A, 41, 555
Balbus, S. A., & Hawley, J. F. 1991, ApJ, 376, 214
Blandford, R. D., & Begelman, M. C. 1999, MNRAS, 303, L1
Blandford, R. D., & Payne, D. G. 1982, MNRAS, 199, 883
Casse, F., & Keppens, R. 2002, ApJ, 581, 988
Contopoulos, J. 1995, ApJ, 450, 616
Ebisawa, K. 1999, in ASP Conf. Ser. 161, High Energy Processes in Accreting Black Holes, ed. J. Poutanen & R. Svensson (San Francisco: ASP), 39
Fukue, J. 1990, PASJ, 42, 793
Fukue, J., Shibata, K., & Okada, R. 1991, PASJ, 43, 131
Galeev, A. A., Rosner, R., & Vaiana, G. S. 1979, ApJ, 229, 318
Hawley, J. F. 2000, ApJ, 528, 462
———. 2001, ApJ, 554, 534
Hawley, J. F., & Balbus, S. A. 2002, ApJ, 573, 738 (HB02)
Hawley, J. F., Balbus, S. A., & Stone, J. M. 2001, ApJ, 554, L49
Hawley, J. F., & Krolik, J. H. 2001, ApJ, 548, 348
Ichimaru, S. 1977, ApJ, 214, 840
Igumenshchev, I. V., Narayan, R., & Abramowicz, M. A. 2003, ApJ, 592, 1042 (INA03)
Igumenshchev, R., & Abramowicz, M. A. 2000, ApJS, 130, 463
Igumenshchev, R., Abramowicz, M. A., & Narayan, R. 2000, ApJ, 537, L27
Kato, S., Fukue, J., & Mineshige, S. 1998, in Black Hole Accretion Disks, ed. S. Kato, J. Fukue, & S. Mineshige (Kyoto: Kyoto Univ. Press), chap. 10
Kato, Y., Hayashi, M. R., & Matsumoto, R. 2004, ApJ, in press
Klein-Wolt, M., Fender, R. P., Pooley, G. G., Belloni, T., Migliari, S., Morgan, E. H., & van der Klis, M. 2002, MNRAS, 331, 745
Kruskal, M., & Schwarzschild, M. 1954, Proc. R. Soc. London A, 223, 348
Kudoh, T., Matsumoto, R., & Shibata, K. 1998, ApJ, 508, 186
———. 2002, PASJ, 54, 267 (KMS02)
Liu, B. F., Mineshige, S., & Shibata, K. 2002, ApJ, 572, L173
Lovelace, R. V. E., Wang, J. C. L., & Sulkanen, M. E. 1987, ApJ, 315, 504
Lynden-Bell, D. 1996, MNRAS, 279, 389
Lynden-Bell, D., & Boily, C. 1994, MNRAS, 267, 146
Machida, M., Hayashi, M. R., & Matsumoto, R. 2000, ApJ, 532, L67
Machida, M., & Matsumoto, R. 2003, ApJ, 585, 429
Machida, M., Matsumoto, R., & Mineshige, S. 2001, PASJ, 53, L1
Matsumoto, R. 1999, in Numerical Astrophysics, ed. S. M. Miyama, K. Tomisaka, & T. Hanawa (Dordrecht: Kluwer), 195
Matsumoto, R., Horiuchi, T., Shibata, K., & Hanawa, T. 1988, PASJ, 40, 171
Matsumoto, R., Uchida, Y., Hirose, S., Shibata, K., Hayashi, M. R., Ferrari, A., Bodo, G., & Norman, C. 1996, ApJ, 461, 115
Mineshige, S., Kusnose, M., & Matsumoto, R. 1995, ApJ, 445, L43
Narayan, R. 2002, in Lighthouses of the Universe, ed. M. Gilfanov, R. Sunyaev, & E. Churazov (Berlin: Springer), 405
Narayan, R., Mahadevan, R., & Quataert, E. 1998, in Theory of Black Hole Accretion Disks, ed. M. A. Abramowicz, G. Bjornsson, & J. E. Pringle (Cambridge: Cambridge Univ. Press), 148
Narayan, R., & Yi, I. 1994, ApJ, 428, L13
———. 1995, ApJ, 452, 710
Paczyński, B., & Wiita, P. J. 1980, A&A, 88, 23
Parker, E. N. 1966, ApJ, 145, 811
Pudritz, R. E., & Norman, C. A. 1986, ApJ, 301, 571
Quataert, E., & Gruzinov, A. 2000, ApJ, 539, 809
Richtmyer, R. D., & Morton, K. W. 1967, Interscience Tracts in Pure and Applied Mathematics (2d ed.; New York: Wiley)
Rubin, E. L., & Burstein, S. Z. 1967, J. Comput. Phys., 2, 178
Shapiro, S. L., Lightman, A. P., & Eardley, D. M. 1976, ApJ, 204, 187
Shibata, K., Tajima, T., & Matsumoto, R. 1990, ApJ, 350, 295
Shibata, K., & Uchida, Y. 1985, PASJ, 37, 31
———. 1986, PASJ, 38, 631
Spruit, H. C., Foglizzo, T., & Stehle, R. 1997, MNRAS, 288, 333
Stone, J. M., & Pringle, J. E. 2001, MNRAS, 322, 461
Stone, J. M., Pringle, J. E., & Begelman, M. C. 1999, MNRAS, 310, 1002
Turner, N. J., Bodenheimer, P., & Różyczka, M. 1999, ApJ, 524, 129
Uchida, Y., & Shibata, K. 1985, PASJ, 37, 515
Wang, Y.-M., & Nepveu, M. 1983, A&A, 118, 267
Yokoyama, T., & Shibata, K. 1994, ApJ, 436, L197